Computational Particle Mechanics (2022) 9:969–985
https://doi.org/10.1007/s40571-021-00451-9

A DEM approach for simulating flexible beam elements with the Project Chrono core module in DualSPHysics

Salvatore Capasso[1] · Bonaventura Tagliafierro[2] · Iván Martínez-Estévez[3] · José M. Domínguez[3] · Alejandro J. C. Crespo[3] · Giacomo Viccione[1]

Received: 31 July 2021 / Revised: 6 November 2021 / Accepted: 30 November 2021 / Published online: 29 January 2022

Abstract
This work presents a novel approach for simulating elastic beam elements in DualSPHysics leveraging functions made available by the coupling with the Project Chrono library. Such numerical frameworks, belonging to the Meshfree Particle Methods family, stand out for several features, like complex multiphase phenomena, moving boundaries, and high deformations which are handled with relative ease and reasonable numerical stability and reliability. Based on a co-rotating rigid element structure and lumped elasticity, a cogent mathematical formulation, relying on the Euler–Bernoulli beam theory for the structural discretization, is presented and applied to simulating two-dimensional flexible beams with the discrete elements method (DEM) formulation. Three test cases are presented to validate the smoothed particle hydrodynamics-based (SPH) structure model in both accuracy and stability, starting from an equilibrium test, to the dynamic response, and closing with a fluid–structure interaction simulation. This work proves that the developed theory can be used within a Lagrangian framework, using the features provided by a DEM solver, overtaking the initial limitations, and hence applying the results of static theories to complex dynamic problems.

Keywords SPH · DualSPHysics · Project Chrono · Euler–Bernoulli · DEM · FSI

1 Introduction

Dynamics impacts between fluid flows and structures constitute a serious threat to the safety of marine and coastal structures, and a challenging task for numerical simulations; these phenomena can exert extreme forces on structures, followed by likewise extreme deformations, and, thus, serious structural damages. Fluid–structure interaction (FSI) problems have been traditionally addressed through mesh-based methods [1–3], considering a partitioned approach and using an appropriate finite element method (FEM) to treat the fluid and the structure separately. However, the fluid mesh must follow the movement of the solid, thus making the use of re-meshing tools essential. Computational costs and convergence issues led to exploring alternative mesh-less approaches. Lagrangian methods, in which particles constitute the physical system and move according to the field laws in the local frame of reference, are naturally structured to avoid the common drawbacks of grid-based methods, providing a robust computational tool to enhance the fluid phase simulation in FSI problems. These methods, in fact, can eas-

✉ Salvatore Capasso
scapasso@unisa.it

Bonaventura Tagliafierro
btagliafierro@unisa.it

Iván Martínez-Estévez
ivan.martinez.estevez@uvigo.es

José M. Domínguez
jmdominguez@uvigo.es

Alejandro J. C. Crespo
alexbexe@uvigo.es

Giacomo Viccione
gviccion@unisa.it

1 Environmental and Maritime Hydraulics Laboratory (LIDAM), Università degli Studi di Salerno, Via Giovanni Paolo II 132, 84084 Fisciano, (SA), Italy

2 Department of Civil Engineering (DiCIV), Università degli Studi di Salerno, Via Giovanni Paolo II 132, 84084 Fisciano, SA, Italy

3 Environmental Physics Laboratory, CIM-UVIGO, Universidade de Vigo, Ourense, Spain

ily address large deformation and track complex and moving interfaces between solid and fluid phases.

One of the Lagrangian approaches, which has been gaining interest in recent years, is the smoothed particle hydrodynamics (SPH) method [4], especially regarding coastal engineering applications [5], but in general in all fluid-related fields [6,7]. The SPH approach has been used for solving FSI, where both fluids and solids are modeled within the same SPH framework, however employing different techniques. For example, the coupled enhanced ISPH-SPH method presented in Khayyer et al. [8], which provides full validation for the SPH-based solid solver. Another fully Lagrangian FSI solver has been proposed by Sun et al. [9], by coupling a multi-phase delta-SPH solver for fluid and a total Lagrangian SPH as a solid solver; an improved version of the code is presented in Sun et al. [10]; a weakly compressible SPH solver for fluid dynamics with kernel correction and an hourglass suppression algorithm implemented in SPH as well for structural dynamics is presented in O'Connor and Rogers [11]. Another piece of research by Khayyer et al. [12] reports on an ISPH system coupled to a Hamiltonian SPH (HSPH) structure model resulting in ISPH-HSPH FSI solver, applied for the simulation of laminated, composite structures.

Due to their flexibility, meshfree methods can embed framework with different nature. One such example is the use of the SPH technique for meshless-to-mesh-based couplings, where the Lagrangian solver is mainly used to deal with fluids. A recent research dealing with an SPH-FEM for FSI can be found in Li et al. [13]: the newly formed hybrid framework benefits from the strengths of both. Some applications of this methodology are presented in Fourey et al. [14]. Another interesting strategy is to couple a Lagrangian discrete element method (DEM) to an SPH solver. It is either used to studying the dynamics of multi-body systems [15–17, see] or to simulating flexible objects by composing mass-spring elements to form complex geometries [18–20, see]. The mathematical structure of the proposed method follows a partitioned approach with two different solvers operating in co-simulation.

At the basis of the present model lies the discrete element method, developed to simulate the behavior of interacting discrete bodies. DEM is becoming widely accepted as an effective method for addressing problems in civil engineering, even though FEM-based codes remain unrivaled when dealing with small elastic deformations or vibrations. The DEM approach, nevertheless, being based on the interacting force computation between rigid bodies, is suitable for phenomena involving breakage, rupture and large deformations, together with contacts of multiple bodies [21]. Its features perfectly fit the lumped elasticity model here proposed that relies on a set of rigid bodies, and allow the straightforward computation of both interactions within the rigid elements set and with the fluid phase for simulating FSI.

DualSPHysics is an open-source computer software available at http://www.dual.sphysics.org, released under the GNU Lesser General Public License (LGPL), based on the SPH method [22]. The capability of DualSPHysics to address complex multiphysics applications has been enhanced by the coupling with other numerical models. These include coupling with wave propagation models, such as SWASH and OceanWave3D [23,24], coupling with the MoorDyn mooring library [25], coupling with distributed-contact discrete element method (DCDEM)[26] and coupling with Project Chrono library [15]. Thanks to the latter coupling to the Project Chrono multiphysics library [27], the DualSPHysics framework can simulate complex mechanical systems and multi-body problems. Canelas et al. [15] showed a complete coupling validation for the multibody dynamics simulator [25,28]; Brito et al. [29] presented a set of mechanical constraints and then validated their use contrasting numerical and experimental results for an oscillating wave surge converter device. Within the field of renewable energy, many successful applications have been presented over the last years [30–34].

A novel approach for simulating flexible elements is here presented, built upon the preliminary research study presented in [35]. The model leverages Lagrangian features and relies on the effectiveness of the DualSPHysics–Project Chrono fluid–solid interactive solver. Starting from the Euler–Bernoulli beam theory [36], a robust lumped elasticity formulation is developed, calibrated, and successively implemented in the software; the procedure is finally validated with several test cases proving a thorough assessment of the accuracy of the SPH-DEM-based numerical framework.

This work is structured as follows: in Sect. 2, the SPH formulation for the governing equations implemented in DualSPHysics is presented, together with the coupling to the Project Chrono library; in Sect. 3, the mathematical formulation is reported, from the starting assumptions to the numerical discretization; in Sect. 4, several validation benchmark cases provide the performance of the model in simulating FSI phenomena; Sect. 5 summarizes the main results for this research.

2 DualSPHysics solver

The SPH numerical method is based on the use of a *kernel* function which is suitable for representing the derivatives of continuous fields in a discrete form. The resulting equations then consist of discrete mechanical systems, in which the interactions between particles are expressed by fluxes which depend, in particular, on their mutual distances and their mechanical and thermodynamic features. The discrete treatment of time makes SPH a fully conservative method [37].

2.1 SPH formulation

The strategy in SPH is to discretize the physical domain (fluid and/or solid objects) into a set of particles, where the physical quantities (position, velocity, density and pressure) are obtained as an interpolation of the corresponding quantities of the surrounding particles. The contribution of those particles is weighted using a kernel function, with an area of influence that is defined using a characteristic *smoothing length*. This discretization process is divided into two key steps [38].

The first step is the integral representation or the so-called kernel approximation of field functions, consisting in the integration of a multiplication of an arbitrary function and a smoothing kernel function. The integral representation of a generic spatial function $f(\mathbf{r})$ within an integral volume $\boldsymbol{\Omega}$ is given by:

$$< f(\mathbf{r}) >= \int_{\Omega} f(\mathbf{r}')W(\mathbf{r}-\mathbf{r}', h)\mathrm{d}\mathbf{r}', \tag{1}$$

where W is the so-called *smoothing kernel function* or *kernel*. In the smoothing function, h is the smoothing length defining the influence area of W (Fig. 1).

Then, the second step follows, in which the integral representation is approximated by summing up the values of the nearest neighbor particles, which yields the particle approximation of the function at a discrete point (particle). The position $\mathbf{r}_b$ is defined as the position of a particle having a fixed mass m_b and a finite volume V_b, related by:

$$V_b = \frac{m_b}{\rho_b}, \tag{2}$$

where ρ_b is the density of particle $b = 1, \ldots, N_p$ in which N_p is the total number of particles within the support domain of particle a. The integral representation can be rewritten in a discrete form for a particle a, being b part of its support domain:

$$< f(\mathbf{r}_a) >= \sum_{b=1}^{N_p} \frac{m_b}{\rho_b} f(\mathbf{r}_b)W_{ab}, \tag{3}$$

where:

$$W_{ab} = W(\mathbf{r}_a - \mathbf{r}_b, h). \tag{4}$$

The kernel function, hence, plays a fundamental role in the SPH method. In DualSPHysics, the Wendland [39] quintic kernel function is utilized:

$$W(r,h) = \alpha_{D,n} \begin{cases} \left(1-\frac{q}{2}\right)^4 (1+2q) & 0 \le q \le 2 \\ 0 & 2 < q, \end{cases} \tag{5}$$

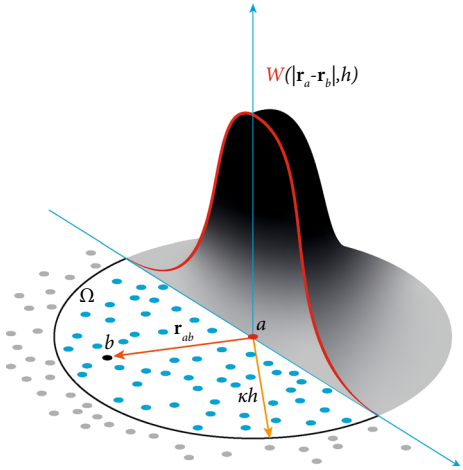

Fig. 1 Representation of smoothing kernel function for two-dimensional frameworks

where

$$q = \frac{r}{h} = \frac{|\mathbf{r}-\mathbf{r}'|}{h}, \tag{6}$$

and $\alpha_{D,n}$ is a constant depending on the spatial dimension of the problem.

2.2 Governing equations

The governing equations for a fluid domain in Lagrangian formulation and the relative SPH discretization are herein presented. The equations of fluid dynamics are based on the fundamental physical laws of conservation: the conservation of mass and momentum. These laws yield, respectively, to the continuity equation:

$$\frac{D\rho}{Dt} = -\rho\nabla\cdot\mathbf{u}, \tag{7}$$

and the momentum equation:

$$\frac{D\mathbf{u}}{Dt} = -\frac{1}{\rho}\nabla p + \mathbf{g} + \boldsymbol{\Gamma}, \tag{8}$$

where ρ is the density, $\mathbf{u}$ is the velocity vector, $\mathbf{g}$ the gravitational acceleration, p is the pressure, and $\boldsymbol{\Gamma}$ is the divergence of the deviatoric stress tensor. In the weakly compressible SPH (WCSPH), the governing equation formulation implemented in DualSPHysics becomes:

$$\frac{D\rho_a}{Dt} = \sum_{b=1}^{N_p} m_b\mathbf{u}_{ab}\cdot\nabla_a W_{ab} + \delta_\Phi hc_0 \sum_{b=1}^{N_p} \Psi_{ab}\cdot\nabla_a W_{ab}\frac{m_b}{\rho_b}, \tag{9}$$

$$\frac{D\mathbf{u}_a}{Dt} = -\sum_{b=1}^{N_p} m_b\left(\frac{p_b+p_a}{\rho_a\rho_b} + \Pi_{ab}\right)\cdot\nabla_a W_{ab} + \mathbf{g}. \tag{10}$$

The SPH continuity equation (Eq. (9)) is enhanced by adding a density diffusion term (DDT) governed by δ_Φ, which is a parameter usually set equal to 0.10, and by the term

$$\Psi_{ab} = 2\left(\rho_b^D - \rho_a^D\right)\frac{\mathbf{r}_{ab}}{|\mathbf{r}_{ab}|}, \tag{11}$$

where the superscript ^{D} indicates the dynamic pressure (i.e., the difference between the total and the hydrostatic pressure). Originally introduced by Molteni and Colagrossi [40] and further developed by Fourtakas et al. [41] by improving the efficiency of the diffusive term near to the boundaries, this formulation helps reduce density fluctuations in the pressure field, which often occur using a weakly compressible approach.

In Eq. (10), the term:

$$\Pi_{ab} = \alpha_{D,n}\begin{cases} \dfrac{-\alpha\overline{c}_{ab}\mu_{ab}}{\overline{\rho}_{ab}} & \boldsymbol{u}_{ab}\cdot\boldsymbol{r}_{ab} < 0, \\ 0 & \boldsymbol{u}_{ab}\cdot\boldsymbol{r}_{ab} > 0, \end{cases} \tag{12}$$

where:

$$\begin{aligned} \mu_{ab} &= \frac{h\mathbf{u}_{ab}\cdot\mathbf{r}_{ab}}{|\mathbf{r}_{ab}|^2+\eta^2}, \\ \overline{c}_{ab} &= \frac{1}{2}(c_a + c_b), \\ \overline{\rho}_{ab} &= \frac{1}{2}(\rho_a + \rho_b), \text{ and} \\ \eta^2 &= 0.01h^2, \end{aligned} \tag{13}$$

is added to the physical pressure term to help diffuse sharp variation in the flow and dissipate the energy of high-frequency terms. This artificial viscosity term numerically reproduces, as a form of viscous dissipation, particular phenomena of hydrodynamics problems, like shock waves, in which sudden transformation of kinetic energy into heat energy occurs [38].

In Eq. (13), $\overline{c}_{ab}$ and $\overline{\rho}_{ab}$ are the mean speed of sound and mean pressure value respectively, while α is a constant that needs to be tuned in order to introduce the proper dissipation. The fluid, in the SPH formalism defined in DualSPHysics, is treated as *weakly compressible* [42] due to an equation of state (Eq. (14)) that is used to determine fluid pressure based on particles density. The fluid compressibility is adjusted so that the speed of sound can be artificially lowered; this means that the size of the time steps taken at any one moment (which is determined according to a Courant–Friedrich–Lewy (CFL) condition, and based on the currently maximum speed for all particles) can be maintained at a reasonable value. Such adjustment, however, restricts the sound speed to be at least ten times faster than the maximum fluid velocity, keeping density variations to be within less than 1%, and therefore not introducing major deviations from an incompressible approach [38]. The state equation [42]:

$$p = \frac{c_0^2\rho_0}{\gamma}\left[\left(\frac{\rho}{\rho_0}\right)^\gamma - 1\right], \tag{14}$$

where $\gamma = 7$, $\rho_0 = 1000$ [kg/m^3], $c_0 = c(\rho_0)$, c being the numerical speed of sound, along with Eqs. (9) and (10) completes the set of governing equations for the fluid domain implemented in DualSPHysics [22].

2.3 Modified dynamic boundary conditions

DualSPHysics implements the dynamic boundary condition (DBC), proposed by Crespo et al. [43], as a standard method for the definition of the boundary conditions. The DBC treatment has demonstrated to work properly when applied to cases of wave propagation, wave run-up of armor block breakwaters with complex geometries [44], and also simulating violent collisions with coastal structures [45]. However, a novel formulation was proposed [46] in order to improve the initial DBC formulation, solving the over dissipation of the former approach when the transition from non-wet to wet bound takes place. The modification of DBCs (the so-called mDBCs) works with the same particle arrangement defined for its parent version, but the interacting boundary surface is located away from the outermost layer of particles. This latter location is used to mirror ghost nodes into the fluid domain and hence evaluating the fluid properties at that virtual position; eventually, these properties are used to correct the SPH approximation when a fluid particle interacts with a mDBC particle, as it was already performed in [47]. mDBCs are validated in the reference paper of English et al. [46], and an application is presented in Capasso et al. [48].

2.4 Rigid body dynamics and SPH

A full SPH model can deal with rigid bodies by computing the total force contributions of the surrounding fluid particles. In DualSPHysics, the motion of objects interacting with fluid particles is handled by the basic equations of rigid body dynamics. By assuming that a body is rigid, the net force on each boundary particle is computed according to the designated kernel function and smoothing length. Each boundary particle k experiences a force per unit mass given by:

$$\boldsymbol{f}_k = \sum_{b\in fluid} \boldsymbol{f}_{kb}, \tag{15}$$

where $\boldsymbol{f}_{kb}$ is the force per unit mass exerted by the fluid particle b on the boundary particle k. For the motion of rigid

bodies, the basic equations of rigid body dynamics can then be used:

$$\boldsymbol{M}\frac{\mathrm{d}\boldsymbol{V}}{\mathrm{d}t} = \sum_{k\in body} m_k \boldsymbol{f}_k, \text{ and} \tag{16}$$

$$\boldsymbol{I}\frac{\mathrm{d}\boldsymbol{\Omega}}{\mathrm{d}t} = \sum_{k\in body} m_k(\boldsymbol{r}_k - \boldsymbol{r}_0) \wedge \boldsymbol{f}_k, \tag{17}$$

where $\boldsymbol{M}$ is the mass of the object, $\boldsymbol{I}$ is the moment of inertia, $\boldsymbol{V}$ is the linear velocity, $\boldsymbol{\Omega}$ the angular velocity, $\boldsymbol{r}_k$ position of the particle k, and $\boldsymbol{r}_0$ the center of mass; $\wedge$ indicates the cross-product. Equations (16) and (17) are integrated in time to predict the values of $\boldsymbol{V}$ and $\boldsymbol{\Omega}$ at the beginning of the next time step. Each boundary particle within the body has a velocity given by:

$$\boldsymbol{v}_k = \boldsymbol{V} + \boldsymbol{\Omega} \wedge (\boldsymbol{r}_k - \boldsymbol{r}_0). \tag{18}$$

Finally, the boundary particles within the rigid body are moved by integrating Eq. (18) in time. The presented formulation for the dynamics of rigid bodies was proposed and validated in Monaghan et al. [49], which shows that linear and angular momentum are conservative properties. Validations about buoyancy-driven motion are performed in Domínguez et al., [25].

2.5 Coupling with Project Chrono Library

The DualSPHysics framework handles mechanical laws among rigid bodies via the solvers provided by Project Chrono (PC) [50]. The Project Chrono library has been implemented into the original framework, creating an integrated interface for simulating structure–structure interaction as well, using various contact tracing features [51]. The library is primarily developed to handle very large systems of 3D rigid bodies [15]. The coupling allows for arbitrarily shaped bodies to be considered, and the solver can integrate externally applied forces and torques, and the effects of kinematic-type restrictions, dynamic-type restrictions and internal collisions.

Figure 2 summarizes the implementation strategy; DualSPHysics computes the linear and angular acceleration of floating objects following the interaction with fluid particles, passing the information $\{\frac{\mathrm{d}\boldsymbol{V}}{\mathrm{d}t}; \frac{\mathrm{d}\boldsymbol{\Omega}}{\mathrm{d}t}\}$ to the Chrono module that integrates in time (using smaller time steps Δt_{CHR}), the active ($\boldsymbol{F}_A$) and reactive ($\boldsymbol{F}_R$) forces exerted on bodies, according to the Chrono scheme presented in Fig. 4. The position $\mathbf{R}$, angular Ω and linear velocity $\mathbf{V}$ computed by Chrono are used by DualSPHysics to update the data of the floating particles belonging to each floating object.

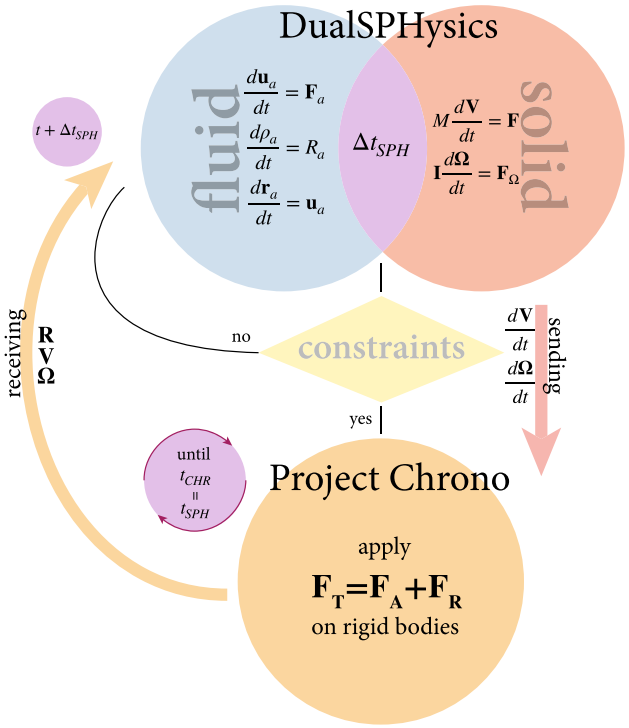

Fig. 2 Schematic flowchart of the coupled DualSPHysics–Project Chrono code

The coupled DualSPHysics–Chrono code is employed in this work to implement the DEM approach that is developed in Sect. 3. The connection between the two following rigid bodies (trunks) is managed by a rotational hinge, which applies a bending moment according to:

$$M(t) = \zeta\dot{\theta}(t) + k\theta(t), \tag{19}$$

where ζ is the rotational damping, θ is the relative rotation between two points, k is the rotational stiffness.

3 Co-rotating rigid beam

The widely used structural static theories compute deformation according to the internal stress of beams [52] solving ordinary differential equations (ODE). These equations are derived for thin beams according to the Euler–Bernoulli (EB) hypotheses, combining kinematics and linear elasticity. The former parameters can be resumed by the generalized functions:

$$\begin{aligned} v &= v(z), \\ \varphi(z) &= -\frac{\mathrm{d}v(z)}{\mathrm{d}z}; \end{aligned} \tag{20}$$

which represent the *vertical displacement* and *rotation function* of each cross section along the beam axis z, respectively.

The linear elasticity theory, rather, links the kinematics to the internal stress with the so-called *constitutive bonds*, among which we consider only the flexural one:

$$\frac{\mathrm{d}\varphi(z)}{\mathrm{d}z} = \frac{M}{EI}, \tag{21}$$

with M being the bending moment, E the Young's Modulus, ans I the second moment of inertia of the cross section.

In this work, to numerically implement this formulation, an equilibrium-based approach is followed, which allows the direct extension of the model to the dynamic framework of DualSPHysics. The approach is formulated on the dynamics of rigid bodies, with suitably tuned reciprocal rotational constraints to reproduce the behavior of one-dimensional elastic elements. The flexible beam is composed of several trunks connected by rotational hinges, whose motion is defined by the rotation values in each of the relative constraints [35,53].

3.1 Numerical discretization

Being the focus of this study on elastic beams in an SPH-based framework, the numerical discretization of the governing equation for bending beams is purposely developed to allow its use for simulating dynamic phenomena. The EB formulation is well-established and widely used in the statical structural analysis; by only considering the flexural behavior of the beam costs a limited error in most of engineering applications.

To begin with, the vertical displacement function $v = v(z)$ can be discretized, with the finite element representation, as a series of local defined low-order functions ψ_i which interpolates between the $v_i = v(i)$ values:

$$v(z) \approx \sum_i \psi_i v_i, \text{ with } i = 1, \ldots, N+1. \tag{22}$$

In the case that ψ_i is a first-order polynomial, the approximation is linear, which can be materially represented by rigid elements, hereafter referred as *trunks*. The numerical properties of the interpolation polynomials are physically the position and length of the trunks, whose terminal cross sections locate rotational hinges. The positions of the hinges related to the $j\text{-}th$ trunk, identified, respectively, as i and $i+1$, can be given by a single rotational parameter, namely φ_i (Fig. 3). The displacement u of the point $i+1$ is known once the angle φ_i (rotation in i) is defined; from the rigid body kinematics:

$$\mathbf{u}_{i+1} = \boldsymbol{\varphi}_i \times \mathbf{r}_{i,i+1}, \tag{23}$$

where $r_{i,i+1} = r_{i+1} - r_i \doteq \Delta z_j$, and assuming $\boldsymbol{\varphi} = \{\varphi_i, 0, 0\}$. In the two-dimensional EB framework, it becomes:

$$v_{i+1} = \sin\varphi_i \Delta z_j, \text{ with } j = 1, \ldots, N. \tag{24}$$

The generic hinge abscissa $z(i) \doteq z_i$, with respect to a rectilinear beam of length L and thickness h_b, the z-axis being axis of symmetry in the plane $\{x_2, z\}$ is identified as the beam is divided in N trunks of dimensions:

$$\Delta z = \frac{L}{N}, \tag{25}$$

if the discretization step is constant. The dimension of the beam along x_1 is considered unitary. It is clear that to reproduce the displacement function, the value of the rotation of each trunk is needed, together with simple rigid dynamics considerations.

3.1.1 Discrete constitutive bond

In order to use this numerical discretization in a dynamic framework, a further consideration is needed: the unknown of the problem, φ_i, can be calculated directly from an equilibrium equation if a finite version of the flexural constitutive bond is provided, considering that the bending moment in two consecutive sections is proportional to their relative rotation. When the length of the trunk is small enough, it is possible to assume that $\Delta z \simeq dz$, and thus this rotation value can be considered finite. The passage from infinitesimal to finite quantities,

$$d\varphi \simeq \Delta\varphi = \frac{\Delta z}{EI} M, \tag{26}$$

obviously comes at a cost: the approximation error, and it depends on the number of trunks, as for $N \to \infty$, $\Delta z \to 0$. The obtained finite value of rotation $\Delta\varphi$, being the $j\text{-}th$ trunk rigid, can be lumped in one of its points, namely the rotational hinge i placed on the initial section:

$$\overline{\varphi}_i \frac{EI}{\Delta z_{j=i}} = M_i, \tag{27}$$

where $\overline{\varphi}_i$ is the local rotation and M_i is the total reactive moment. Once the length of the trunk is assigned, the constant quantities can be isolated and named *rotational stiffness* of the generic hinge:

$$K_{\varphi,i} \doteq \frac{EI}{\Delta z_{j=i}}. \tag{28}$$

Equation (27) describes the rotation of every trunk that composes the beam; knowing its mechanical and geometrical

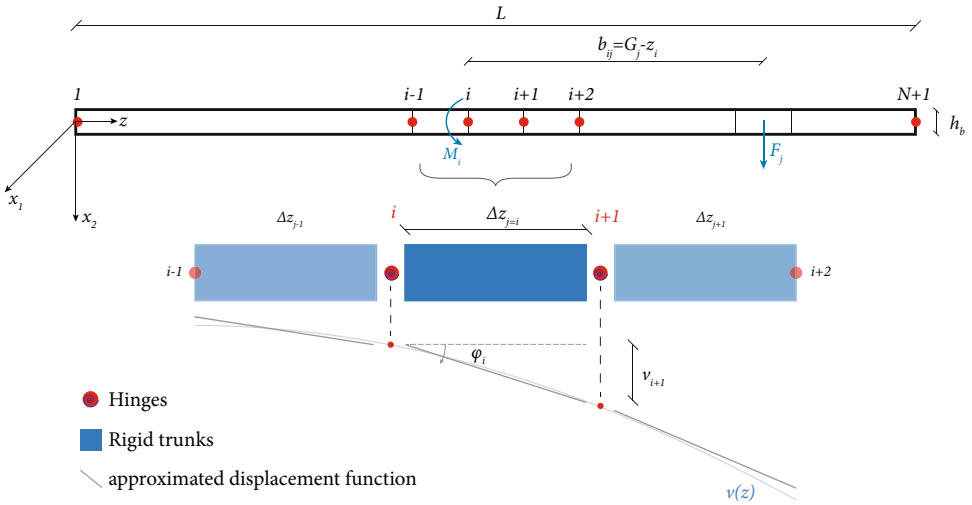

Fig. 3 General discretization scheme of one-dimensional beams: the significant quantities are displayed

characteristics, and the moment applied at the generic hinge, it yields:

$$M_i \doteq \sum_{k=j}^{N} M_{ik} = \sum_{k=j}^{N} b_{ik} F_k, \tag{29}$$

where F_j is the resultant of the forces applied on Δz_j, and b_{ij} is the lever arm, defined as the distance between the $i\text{-}th$ hinge of coordinate z_i and the center of gravity of the $j\text{-}th$ trunk of coordinate G_j.

3.1.2 Co-rotating cantilevered beam

The proposed numerical model is developed for a *cantilevered* beam, and this static scheme will be utilized for validations.

Boundary conditions The BCs for the aforementioned scheme need to be imposed. The first trunk presents one fixed cross section, so its rotation is null, while the remaining sections can rotate; the displacement and rotation values in the leftmost cross section ($z = 0$) follow:

$$\begin{aligned} &v|_{z=0} = 0, \text{ and} \\ &v'|_{z=0} = 0 = 0. \end{aligned} \tag{30}$$

However, this condition is not fully utilized: a hinge is used in its stead, which fulfills the condition on the linear displacement, but not on the rotation. To motivate this choice, let us consider the second hinge: this point has abscissa $z = \Delta z$ with a nonzero vertical displacement, provided by Eq. (27). The equation's dependence is given by only $\varphi_{i=1}$, which is null only when $M_1 = 0$. Having the first trunk a finite dimension and by considering it entirely fixed may cause the numerical solution to have an initial, unrecoverable error, due to the BC on the v'. This last geometrically corresponds to a point with horizontal tangent. Since the number of trunks N is also a computational parameter, the dimension of Δz is usually large to be used as a finite representation of the tangent in $z = 0$. Thus, $\varphi_{i=1}$ can be evaluated considering the bending deformation of a semi-fixed trunk.

The flexural constitutive bond provides that the bending moments acting on both cross sections $\Sigma(z)$ and $\Sigma(z + dz)$ are equal, and, as a first approximation, it can be considered constant along Δz too. Therefore, the bending moment, being the only nonzero component of the generalized tension, leads to assume that the rotations of the ending sections of each trunk are symmetrical. When one of these sections is fixed, the resulting rotation belongs to the deformable section only. Thus, the rotation is halved, and it can be considered as belonging to a trunk with length $\frac{\Delta z}{2}$. The rotational stiffness of the first trunk, hence, is:

$$K_{\varphi,i=1} \doteq \frac{2EI}{\Delta z_{j=i}}. \tag{31}$$

Displacement function Thanks to the rigid body kinematics, the vertical displacement function can be built by solving the N equilibrium equations for the N hinges. Let

$$\varphi_i = \sum_{k=1}^{i} \overline{\varphi}_k \tag{32}$$

be the total rotation of the $i\text{-}th$ hinge; thus,

$$\overline{v}_{i+1} = \Delta z_{j=i} \sin \varphi_i \tag{33}$$

is the local vertical displacement of the section z_{i+1}, and

$$v_i = \sum_{k=1}^{i} \overline{v}_k \tag{34}$$

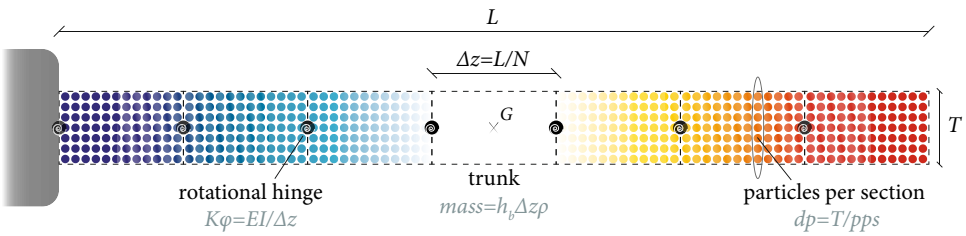

Fig. 4 Scheme of the flexible element composed of rigid bodies (floating objects) and rotational hinges

is the total vertical displacement. This numerical approach, being based on equilibrium (Eq. (27)), can be naturally extended in the dynamic framework of DualSPHysics and Project Chrono, once the governing free parameters N and the stiffness related to each hinge K_ϕ are assigned.

4 Validation

The proposed procedure for modeling flexible objects in DualSPHysics uses the DEM module implemented in the Project Chrono Library. The flexible elements are modeled according to Fig. 4, with rigid objects mutually linked by elastic hinges, characterized by a preimposed value of rotational stiffness. The sensitivity analysis is carried out considering the free parameters:

- N—number of rigid trunks composing the flexible element;
- pps—defined as the number of particles per straight cross section, given as:

$$pps \doteq \frac{T}{dp}, \tag{35}$$

where T is the thickness of the beam, and dp the initial inter-particle distance.

4.1 Equilibrium of a cantilever elastic plate under gravity

The performance of the developed DEM-SPH model is firstly verified by reproducing the static displacement function of a cantilevered elastic beam under gravity. The structural scheme for this test resembles the set of trunks and hinges shown in Fig. 4, in which the axis of the beam can be considered perpendicular to the gravity direction. The results, with respect to resolution and number of trunks, are validated against the elastic line equation (static), which for a cantilevered beam under an uniformly distributed vertical load gives:

$$v_{an}(z) = \frac{qL^2z^2}{4EI} - \frac{qLz^3}{6EI} + \frac{qz^4}{24EI}, \tag{36}$$

Table 1 Physical parameters for the static test from Antoci et al. [55]

Parameter	Plate	Unit
Length (L)	0.079	m
Thickness (T)	0.005	m
Density (ρ_s)	1100	kg/m^3
Young's modulus (E_s)	12.00	MPa
Force per unit of mass (g)	9.81	ms^{-2}

Table 2 Physical parameters for the case proposed in Khayyer et al. [8]

Parameter	Plate	Unit
Length (L)	0.200	m
Thickness (T)	0.020	m
Density (ρ_s)	1000	kg/m^3
Young's modulus (E_s)	2.00	MPa
Poisson ratio (υ)	0.40	–
Force per unit of mass (g)	0.0	ms^{-2}

where q is the distributed load accounting the effects of gravity, E is the Young's modulus, I is the second moment of inertia of the cross section.

The geometrical and mechanics characteristics here utilized are reported in Table 1, which are taken from [54]. The length-to-thickness ratio classifies this cantilevered beam into the class of *long beams*, making it suitable for being described by the EB theory, despite the high deformability due to the low Young's modulus. It is altogether necessary to validate the model with rubber-like materials since all the following benchmarks involve such material. The relative displacement of the cantilever free-end, $\upsilon(L)/L$, is of the order of the 3%, stating the validity of the analytical solution proposed as reference (Eq. 36).

The equilibrium in the DualSPHysics framework is reached thanks to a mild value of damping assigned into Eq. (19) (term ζ), which does not affect the beam final deformed shape. As shown in Fig. 5a, b, the DEM-SPH solver delivers increasing agreement as the number of springs

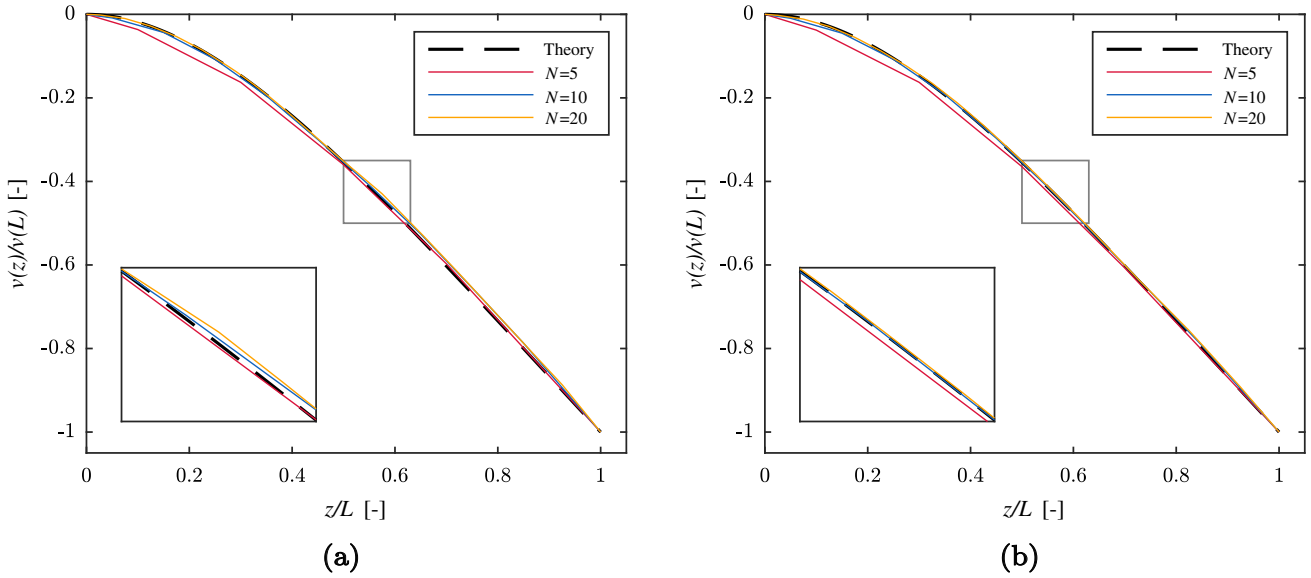

Fig. 5 Displacement function with different number of trunks: $pps = 4$ (**a**) and $pps = 10$ (**b**)

and trunks increases, regardless of pps. The numerical outcome is contrasted against the analytical solution (dashed black line) provided by Eq. (36) by using the mechanical and geometric properties in Table 1. The maximum agreement is achieved when $N = 20$ is used; it shows proper reproduction of the displacement function , with an L_1 error smaller than 0.1% and an L_∞ smaller than 0.2%.

The influence of resolution can be appreciated in the zooms in Fig. 5b, where a perfect match ($L_1 < 0.01\%$) is shown when the initial particle spacing dp is 1/10 of the beam thickness T, whereas in Fig. 5a, with a mean value of resolution, the gap around the centerline of the cantilever appears sensible.

4.2 Free oscillating cantilever elastic beam

In this section, the co-rotating beam is tested under dynamic conditions. The benchmark herein considered is the case first used by Monaghan [56], and more recently in [8], built upon the solution provided in standard text books. The theory of a cantilevered thin oscillating plate with one edge fixed and the other edges free can be found in Landau and Lifšic [36]. A two-dimensional solution of the middle plane line of the system is considered. The geometry of the plate is described by its length L along the z axis, and its thickness T: these dimensions, along with the mechanical properties, are listed in Table 2. It is subjected to an initial velocity distribution, perpendicular to the axis, according to the function:

$$v_z = \xi c_s \frac{f(z)}{f(L)}, \tag{37}$$

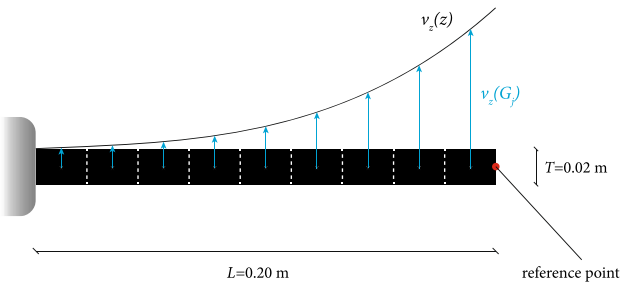

Fig. 6 Discretization scheme of the oscillating cantilever with $N = 10$, and the initial velocity distribution related to each trunk center of gravity

where

$$\begin{aligned} f(z) = &(\cos k_w L + \cosh k_w L) \\ &(\cosh k_w z - \cos k_w z) \\ &+(\sin k_w L - \sinh k_w L) \\ &(\sinh k_w z - \sin k_w z). \end{aligned} \tag{38}$$

In Eq. (37), ξ is equal to 0.01 and c_s is the speed of sound within the body, whereas k_w is the wave number ($k_w L = 1.875$ for the first mode of vibration). The frequency of the oscillation is given by:

$$\omega_1 = (k_w L)^2 \frac{1}{L^2} \sqrt{\frac{EI}{\rho A}}, \tag{39}$$

with the corresponding period being

$$T_1 = \frac{2\pi}{\omega_1}. \tag{40}$$

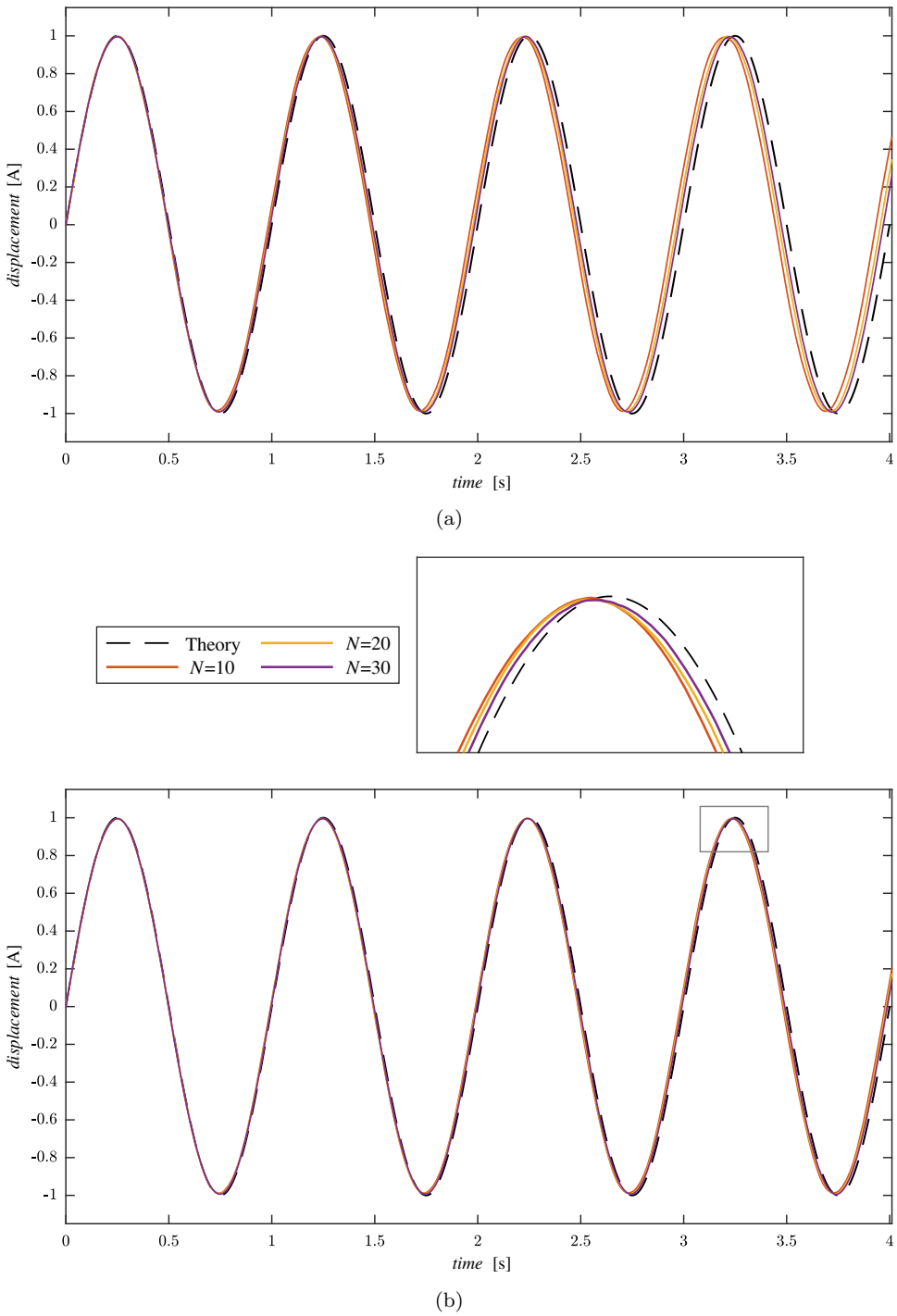

Fig. 7 Time histories of the deflections at the free-end of the oscillating cantilever elastic plate, with $pps = 4$ (**a**) and $pps = 10$ (**b**)

The generic free oscillation analytic function, with respect to the $k-th$ modal form, is given by:

$$u_k(z,t) = [A_k \cos(\omega_k t) + B_k \sin(\omega_k t)] \left(\sin \frac{\omega_k}{H} z\right), \qquad (41)$$

with $H = \sqrt{\frac{E}{\rho}}$; considering the fundamental mode of vibration, it becomes:

$$u_1(z,t) = \frac{\xi c}{\omega_1} \sin(\omega_1 t). \qquad (42)$$

Before discussing the results, it is important to underline that the initial velocity function, obviously defined as continuous (Eq. (37)), is translated in the model applying a numerical velocity value at each trunk's center of gravity depending on their position, as shown in Fig. 6. It follows that not only does the discretization (i.e., the number of elements

Table 3 Period and amplitude error of the free-oscillating cantilever plate benchmark

N	Period error [%]		Amplitude error [%]	
	pps = 4	pps = 10	pps = 4	pps = 10
5	6.99	0.29	3.23	1.39
10	0.29	0.29	0.91	0.82
20	0.29	0.29	0.69	0.61
30	0.29	0.29	0.58	0.60

N) influence the accuracy within the computation process, but also in assigning the initial conditions (IC). Figure 7a, b present the results of the DualSPHysics simulations with two different resolutions. As highlighted in the static test, the agreement increases as the number of trunks and hinges does, and the accuracy is enhanced by higher values of resolution. This may be due to the way the coupling works; the Chrono module evaluates the bodies dynamics using the geometrical properties computed according to the SPH discretization. Thus, a higher resolution guarantees a better reproduction of the geometry. The inset zoom in Fig. 7b highlights the minimum loss of precision after three complete oscillations.

Table 3 presents the period and amplitude errors (L_∞) of the free-oscillating cantilevered plate for the cases shown in Fig. 7, including another case with $N = 5$, which is not reported in the charts for the sake of clarity. Note that the period error remains unchanged, and very limited, over the different N values and for the two resolutions, except for the first simulation. The model correctly addresses the physics of the phenomenon regardless of the number of trunks and of the initial particle spacing. These parameters become relevant when evaluating the amplitude error that decreases with a high number of trunks, and further lowered by finer resolution; the displacement magnitude of the reference point is clearly affected by the discretization parameters.

Table 4 Physical parameters for the case proposed in Liao et al. [54]

Parameter	Plate	Unit
Length (L)	0.090	m
Thickness (T)	0.004	m
Density (ρ_s)	1114	kg/m^3
Young's modulus (E_s)	3.50	MPa
Poisson ratio (υ)	0.50	–
Force per unit of mass (g)	–9.81	ms^{-2}

4.3 FSI validation: Dambreak flow impacting a flexible obstacle

The benchmark proposed by Liao et al. [54] is used to assess the fluid–structure interaction capability of the presented model. The case reproduces a breaking water column impacting a rubber plate in a pseudo two-dimensional confined environment, in which multi-phase effects become relevant for the correct simulation of the obstacle displacement. However, the impact of the water column and the ensuing flow over the flexible obstacle can be accurately simulated for the first 0.80 s of test.

Figure 8 illustrates a lateral view of the simulation set-up, which was designed such that if the dynamics of the fluid and the plate is described by two-dimensional variables,

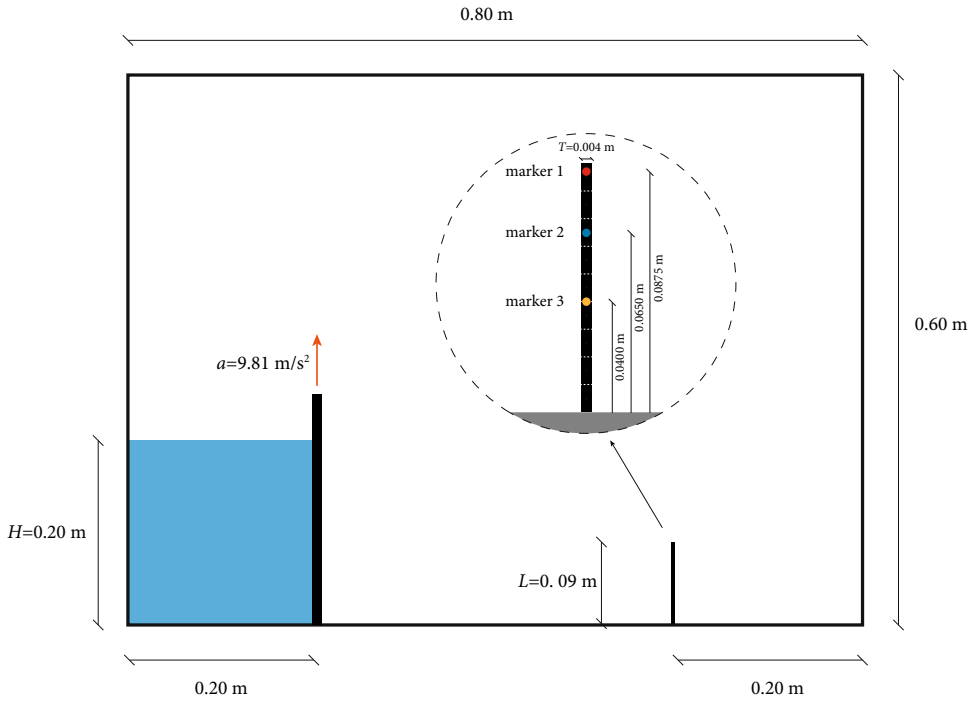

Fig. 8 Geometrical configuration of the dambreak test, with a detailed view of the geometry of the rubber plate

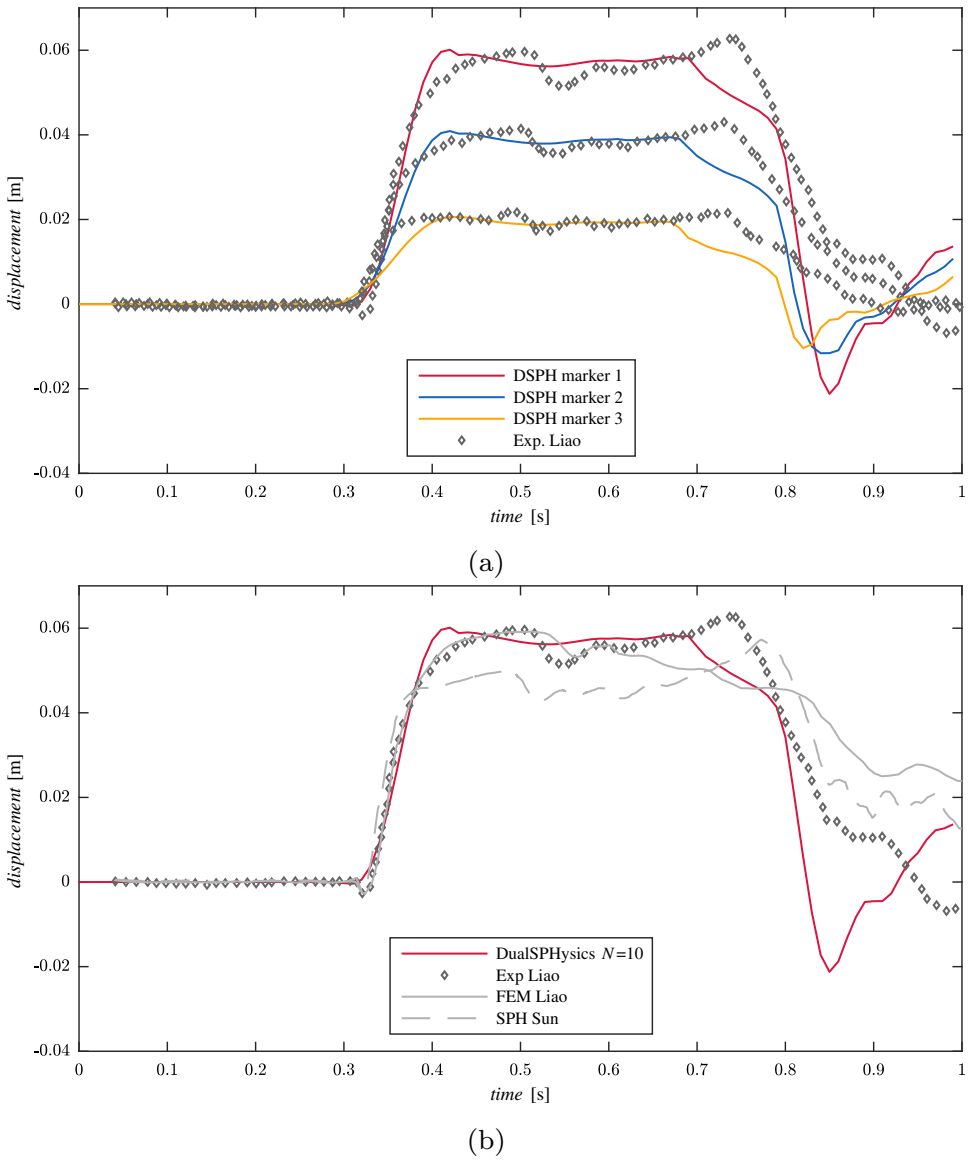

Fig. 9 **a** Horizontal displacement of the three markers with $N = 10$ and $pps = 10$; **b** comparison between the present model and other numerical references [9,54] for the marker #1

the error will be minimized. The water column of 0.20-m height is kept in place by a gate till time $t = 0$ s, when the gate starts moving upward following a gravity-accelerated motion, the law of which was reconstructed by [10] from the original data given in [54]. The geometrical and mechanical characteristics of the flexible obstacle are reported in Table 4; it was equipped, during the experimental campaign, with three markers placed at different heights (highlighted in the zoomed view in Fig. 8), the motion of which is regarded as the main reference parameter to validate the present model.

Prior to the full validation of the proposed FSI simulation procedure, it is convenient to introduce the following corrective procedure. The Young's modulus that is reported in [54] must be corrected to account for the different theories that describe the dynamics of beams and plates. Plate flexural rigidity follows from a different constitutive law, and in order to reproduce the same physics, the following corrected Young's modulus is considered:

$$\hat{E}_s = \frac{E_s}{1-\nu^2}, \tag{43}$$

where $\nu = 0.50$ would be the optimum choice for reproducing rubber-like material behavior. The value of the Young's modulus used to compute the parameters $K_{\varphi,i}$ in Eq. (28) is $\hat{E}_s = 4.67$ MPa.

The SPH particle boundary conditions treatment used for this model is exposed in Sect. 2.3: the use of the mDBCs on every surface, including the flexible obstacle, enhances the simulation as the fluid-phase approaches dry walls, avoiding the small gap observed with the traditional DBCs. This improvement will also provide a more efficient pressure com-

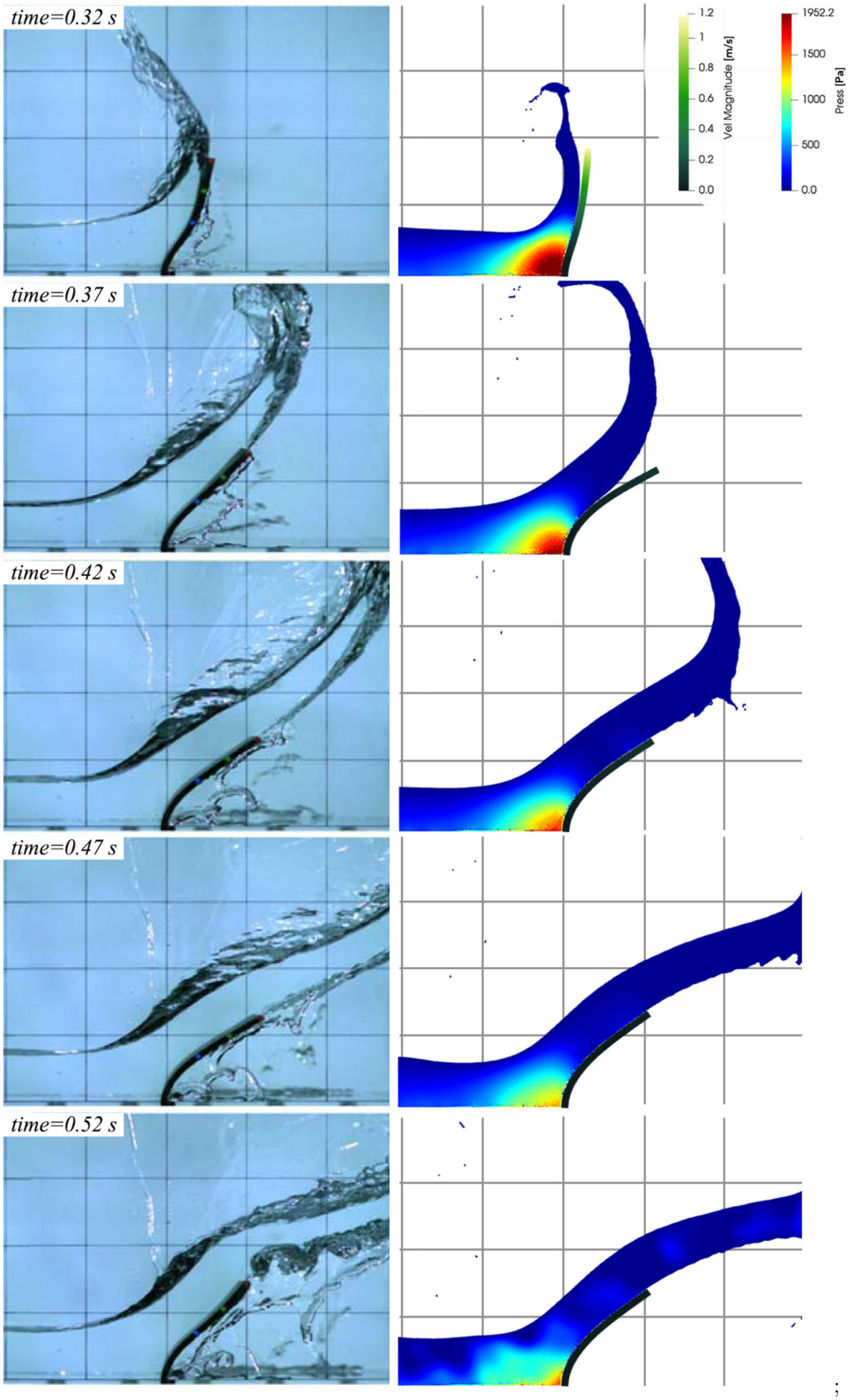

Fig. 10 Dambreak numerical test: comparison between photos from experiment [54] (left column) and the proposed numerical results (right) at different instants of time

putation in further investigations, allowing to deepen the study of this FSI phenomenon.

In Fig. 9a, the horizontal displacement of the three markers is displayed, with $N = 10$ and $pps = 10$: it is possible to notice a small phase delay between the DualSPHysics and experimental results (shifted by 0.04 s), likely due to the gate motion, which also influences the stage of the first impact between the fluid flow and the obstacle (Fig. 10). It results in a slightly different deformed shape when the impact occurs (approximately at $t = 0.32$ s, displayed in Fig. 10), and in the lack of initial negative motion of the first marker, better understandable from Fig. 9b.

After this stage, the results appear in good agreement with the reference, reproducing properly the displacement of the three markers and, hence, the deformed shape of the flexible element. In Fig. 9b, the results for the marker placed near to the free-end are paired with the FEM model from [54] and the multi-phase SPH model from [9]: the proposed DEM-SPH model better reproduces the maximum magnitude of the displacement, while pays in assessing some slight oscillations that may come from higher modes of vibration of the beam. This is due to two reasons: the first, and most important, is that the motion of the obstacle consists in a composition of rotations, being the considered behavior only flexural, and thus it is not possible to reproduce high modes of vibration that include sudden effects from elastic waves propagation. Secondly, the simulations in DualSPHysics are performed in single phase. This specific aspect plays a secondary role in the distribution of forces on to the obstacle — more regular if there were not air cavities within the fluid flow — but it results in a major issue when considering the stage of the second impact; the complex multi-phase flow motion occurring after the impact of the fluid mass with the right-hand side wall is not reproduced in the present simulation, resulting in an accentuated negative motion of the markers (approximately at ($t = 0.85$) s, Fig. 9(b)).

This difference between the models justifies the lack of agreement in the second part of the simulation, where the proposed model is not able to trace the reference results. The SPH-DEM, nevertheless, shows accuracy in addressing such complex applications, being able to properly reproduce the time history of the deformation of the obstacle until the multiphase-related effects remain secondary, as shown in Fig. 10 that reports several screenshots of the first simulation instants. The discretization parameter N does not evidently affects the results, while the resolution dp mainly governs the accuracy of the fluid phase and the fidelity of the forces transferred to the Chrono module. To keep the computational cost at a reasonable level, the simulations were performed with $N = 10$, being the stand-alone beam behavior already validated in Sects. 4.1 and 4.2 with a similar configuration.

5 Conclusions

A novel method based on a lumped elasticity formulation has been developed and implemented within the SPH-based framework of DualSPHysics, augmented with the multibody solver Project Chrono library. The former is able to compute the interaction between fluids and the solid objects that make up flexible elements, whereas the latter provides the solution of the equation of the motion for each object according to active and reactive forces. The behavior of this set of elements is governed by mutual rotational hinges, the stiffness of which is tuned to mimic the flexural behavior of thin one-dimensional elements. This approach makes the most out of the fluid–solid interaction computation capability of the DualSPHysics solver, in which the mutual exchange of forces, pressure, viscous stress between fluid and structure plays a fundamental, and not negligible, role.

Despite the restrictive assumptions of the EB beam theory, which makes it suitable for structures that have limited deformation, it is widely used in nearly all the stages of structural analysis. The presented model relies on the same hypotheses, but has been shown to have a broader application range; in the proposed validations, the flexibility of the rubber-like materials is clearly out of the limitations imposed by the beam theory, but anyway properly reproduced and simulated. This is due to the fact that once the flexible elements relying on the classical two-dimensional elasticity theory are modeled, the deformations of such entities consist of a set of rigid bodies moving in accordance with Newton's equations, particularized with respect to the mutual constraints. High-order effects, necessary when tackling the study of extreme deformations with a theoretical approach, are inherently included into the simulation because of the Lagrangian nature of the environment the elements live in.

In the inherent dynamic framework of DualSPHysics and Project Chrono, the potentialities of the proposed model remarkably raise; the meshfree nature of the SPH method allows extreme deformation with ease, keeping clearly recognizable the interface between fluids and structures without time-costing and laborious re-meshing procedures, aside of a very efficient body force computation, which occurs simultaneously to solid and fluid sets of particles, within the homogeneous simulation domain. The motion of solid bodies computed by the Chrono module, using the forces transmitted by DualSPHysics, completes and defines, with all the aforementioned characteristics, the DEM-SPH numerical model.

The proposed mathematical procedure and the relative numerical approach have been proved to be:

- robust and reliable, in spite of its simplified formulation that omits effects not due to bending moments;
- able to reproduce deformations of elements well out of the limits of the EB theory;

– relatively easy to implement, not requiring modifications in the source codes;
– suitable for reproduce hydroelastic phenomena which involve beam-like structures (e.g., dynamic impacts, time-variant load conditions).

The model has exhibited satisfying agreement in simulating the heterogeneous benchmarks, ensuring good performance in various physical situations, and it motivates to promote enhancing models following the presented approach.

Acknowledgements This work was supported by the project SURVIWEC PID2020-113245RB-I00 financed by MCIN/AEI/10.13039/5011 00011033 and by the project ED431C 2021/44 "Programa de Consolidación e Estructuración de Unidades de Investigación Competitivas" financed by Xunta de Galicia, Consellería de Cultura, Educación e Universidade. B. Tagliafierro acknowledges funding from Italian Ministry for Education, University and Research (MIUR) as part of the program "Dottorati Innovativi a caratterizzazione industriale" (ID DOT 1328490-3). I. Martínez-Estévez acknowledges funding from Xunta de Galicia under "Programa de axudas á etapa predoutoral da Consellería de Cultura, Educación e Universidades da Xunta de Galicia" (ED481A-2021/337). J.M. Domínguez acknowledges funding from Spanish government under the program "Juan de la Cierva-incorporación 2017" (IJCI-2017-32592).

Declarations

Conflict of interest The authors declare that they have no conflict of interest.

References

1. Shadloo MS, Oger G, Le Touzé D (2016) Smoothed particle hydrodynamics method for fluid flows, towards industrial applications: motivations, current state, and challenges. Comput Fluids 136:11–34. https://doi.org/10.1016/j.compfluid.2016.05.029
2. Girfoglio M, Quaini A, Rozza G (2021) Fluid-structure interaction simulations with a LES filtering approach in solids4foam. Commun Appl Ind Math 12(1):13–28. https://doi.org/10.2478/caim-2021-0002
3. Hou G, Wang J, Layton A (2012) Numerical methods for fluid-structure interaction—a review. Commun Comput Phys 12(2):337–377. https://doi.org/10.4208/cicp.291210.290411s
4. Violeau D, Rogers BD (2016) Smoothed particle hydrodynamics (SPH) for free-surface flows: past, present and future. J Hydraul Res 54(1):1–26. https://doi.org/10.1080/00221686.2015.1119209
5. Luo M, Khayyer A, Lin P (2021) Particle methods in ocean and coastal engineering. Appl Ocean Res 114:102734. https://doi.org/10.1016/j.apor.2021.102734
6. Gotoh H, Khayyer A (2018) On the state-of-the-art of particle methods for coastal and ocean engineering. Coastal Eng J 60(1):79–103. https://doi.org/10.1080/21664250.2018.1436243
7. Manenti S, Wang D, Domínguez JM, Li S, Amicarelli A, Albano R (2019) SPH modeling of water-related natural hazards. Water 11:1875. https://doi.org/10.3390/w11091875
8. Khayyer A, Gotoh H, Falahaty H, Shimizu Y (2018) An enhanced ISPH-SPH coupled method for simulation of incompressible fluid-elastic structure interactions. Comput Phys Commun 232:139–164. https://doi.org/10.1016/j.cpc.2018.05.012
9. Sun PN, Le Touzé D, Zhang A-M (2019) Study of a complex fluid-structure dam-breaking benchmark problem using a multi-phase SPH method with APR. Eng Anal Bound Elem 104:240–258. https://doi.org/10.1016/j.enganabound.2019.03.033
10. Sun PN, Le Touzé D, Oger G, Zhang AM (2021) An accurate FSI-SPH modeling of challenging fluid-structure interaction problems in two and three dimensions. Ocean Eng 221:108552. https://doi.org/10.1016/j.oceaneng.2020.108552
11. O'Connor J, Rogers BD (2021) A fluid-structure interaction model for free-surface flows and flexible structures using smoothed particle hydrodynamics on a GPU. J Fluids Struct 104:103312. https://doi.org/10.1016/j.jfluidstructs.2021.103312
12. Khayyer A, Shimizu Y, Gotoh H, Nagashima K (2021) A coupled incompressible SPH-hamiltonian SPH solver for hydroelastic FSI corresponding to composite structures. Appl Math Model 94:242–271. https://doi.org/10.1016/j.apm.2021.01.011
13. Li Z, Leduc J, Nunez-Ramirez J, Combescure A, Marongiu JC (2015) A non-intrusive partitioned approach to couple smoothed particle hydrodynamics and finite element methods for transient fluid-structure interaction problems with large interface motion. Comput Mech 55:697–718. https://doi.org/10.1007/s00466-015-1131-8
14. Fourey G, Hermange C, Le Touzé D, Oger G (2017) An efficient FSI coupling strategy between smoothed particle hydrodynamics and finite element methods. Comput Phys Commun 217:66–81. https://doi.org/10.1016/j.cpc.2017.04.005
15. Canelas RB, Brito M, Feal OG, Domínguez JM, Crespo AJC (2018) Extending dualsphysics with a differential variational inequality: modeling fluid-mechanism interaction. Appl Ocean Res 76:88–97. https://doi.org/10.1016/j.apor.2018.04.015
16. Amicarelli A, Manenti S, Albano R, Agate G, Paggi M, Longoni L, Mirauda D, Ziane L, Viccione G, Todeschini S, Sole A, Baldini LM, Brambilla D, Papini M, Khellaf MC, Tagliafierro B, Sarno L, Pirovano G (2020) Sphera v.9.0.0: a computational fluid dynamics research code, based on the smoothed particle hydrodynamics mesh-less method. Comput Phys Commun 250:107157. https://doi.org/10.1016/j.cpc.2020.107157
17. Asai M, Li Y, Chandra B, Takase S (2021) Fluid-rigid-body interaction simulations and validations using a coupled stabilized ISPH-dem incorporated with the energy-tracking impulse method for multiple-body contacts. Comput Methods Appl Mech Eng 377:113681. https://doi.org/10.1016/j.cma.2021.113681
18. Wu K, Yang D, Wright N (2016) A coupled SPH-dem model for fluid-structure interaction problems with free-surface flow and structural failure. Comput Struct 177:141–161. https://doi.org/10.1016/j.compstruc.2016.08.012
19. Xie F, Zhao W, Wan D (2021) Mps-dem coupling method for interaction between fluid and thin elastic structures. Ocean Eng 236:109449449. https://doi.org/10.1016/j.oceaneng.2021.109449
20. Sun Y, Xi G, Sun Z (2019) A fully Lagrangian method for fluid-structure interaction problems with deformable floating structure. J Fluids Struct 90:379–395. https://doi.org/10.1016/j.jfluidstructs.2019.07.005
21. Fleissner F, Gaugele T, Eberhard P (2007) Applications of the discrete element method in mechanical engineering. Multibody Syst Dyn. https://doi.org/10.1007/s11044-007-9066-2
22. Domínguez JM, Fourtakas G, Altomare C, Canelas R, Tafuni A, Feal OG, Martínez-Estévez I, Mokos A, Vacondio R, Crespo A, Rogers B, Stansby PK, Gómez-Gesteira M (2021) DualSPHysics: from fluid dynamics to multiphysics problems. Comput Part Mech. https://doi.org/10.1007/s40571-021-00404-2
23. Altomare C, Tagliafierro B, Dominguez JM, Suzuki T, Viccione G (2018) Improved relaxation zone method in SPH-based model for coastal engineering applications. Appl Ocean Res 81:15–33. https://doi.org/10.1016/j.apor.2018.09.013

24. Verbrugghe T, Domínguez JM, Altomare C, Tafuni A, Vacondio R, Troch P, Kortenhaus A (2019) Non-linear wave generation and absorption using open boundaries within DualSPHysics. Comput Phys Commun 240:46–59. https://doi.org/10.1016/j.cpc.2019.02.003
25. Domínguez JM, Crespo AJC, Hall M, Altomare C, Wu M, Stratigaki V, Troch P, Cappietti L, Gómez-Gesteira M (2019) SPH simulation of floating structures with moorings. Coastal Eng 153:103560. https://doi.org/10.1016/j.coastaleng.2019.103560
26. Canelas RB, Domínguez JM, Crespo AJC, Gómez-Gesteira M, Ferreira RML (2017) Resolved simulation of a granular-fluid flow with a coupled SPH-DCDEM model. J Hydraul Eng 143(9):06017012. https://doi.org/10.1061/(ASCE)HY.1943-7900.0001331
27. Tasora A, Serban R, Mazhar H, Pazouki A, Melanz D, Fleischmann J, Taylor M, Sugiyama H, Negrut D (2016) Chrono: an open source multi-physics dynamics engine. In: Kozubek T, Blaheta R, Šístek J, Rozložník M, Čermák M (eds) High performance computing in science and engineering. Springer International Publishing, Cham, pp 19–49. https://doi.org/10.1007/978-3-319-40361-8_2
28. Ruffini G, Briganti R, De Girolamo P, Stolle J, Ghiassi B, Castellino M (2021) Numerical modelling of flow-debris interaction during extreme hydrodynamic events with DualSPHysics-CHRONO. Appl Sci. https://doi.org/10.3390/app11083618
29. Brito M, Canelas RB, García-Feal O, Domínguez JM, Crespo AJC, Ferreira RML, Neves MG, Teixeira L (2020) A numerical tool for modelling oscillating wave surge converter with nonlinear mechanical constraints. Renewable Energy 146:2024–2043. https://doi.org/10.1016/j.renene.2019.08.034
30. Ropero-Giralda P, Crespo AJC, Tagliafierro B, Altomare C, Domínguez JM, Gómez-Gesteira M, Viccione G (2020) Efficiency and survivability analysis of a point-absorber wave energy converter using dualsphysics. Renewable Energy 162:1763–1776. https://doi.org/10.1016/j.renene.2020.10.012
31. Tagliafierro B, Montuori R, Vayas I, Ropero-Giralda P, Crespo A, Domìnguez J, Altomare C, Viccione G, Gòmez-Gesteira M (2020) A new open-source solver for modelling fluid-structure interaction: case study of a point-absorber wave energy converter with a power take-off unit. In: Proceedings of the 11th international conference on structural dynamics, Athens, Greece. https://doi.org/10.47964/1120.9052.21578
32. Ropero-Giralda P, Crespo AJC, Coe RG, Tagliafierro B, Domínguez JM, Bacelli G, Gómez-Gesteira M (2021) Modelling a heaving point-absorber with a closed-loop control system using the dualsphysics code. Energies. https://doi.org/10.3390/en14030760
33. Quartier N, Ropero-Giralda P, Domínguez JM, Stratigaki V, Troch P (2021) Influence of the drag force on the average absorbed power of heaving wave energy converters using smoothed particle hydrodynamics. Water. https://doi.org/10.3390/w13030384
34. Quartier N, Crespo AJC, Domínguez JM, Stratigaki V, Troch P (2021) Efficient response of an onshore oscillating water column wave energy converter using a one-phase SPH model coupled with a multiphysics library. Appl Ocean Res 115:102856. https://doi.org/10.1016/j.apor.2021.102856
35. Capasso S, Tagliafierro B, Martínez-Estévez I, Domínguez JM, El Rahi J, Stratigaki V, Crespo AJC, Montuori R, Troch P, Gómez-Gesteira M, Viccione G (2021) On the development of a novel approach for simulating elastic beams in DualSPHysics with the use of the project chrono library. In: Proceedings of the 8th international conference on computational methods in structural dynamics and earthquake engineering, Athens, Greece 28–30 June 2021
36. Landau LD, Lifšic EM (1970) Theory of easticity, vol 7. Pergamon Press, Oxford
37. Violeau D (2012) Fluid mechanics and the SPH method: theory and applications. https://doi.org/10.1093/acprof:oso/9780199655526.001.0001
38. Liu GR, Liu MB (2003) Smoothed particle hydrodynamics. World Scientific, Singapore. https://doi.org/10.1142/5340
39. Wendland H (1995) Piecewise polynomial, positive definite and compactly supported radial basis functions of minimal degree. Adv Comput Math 4(1):389–396. https://doi.org/10.1007/BF02123482
40. Molteni D, Colagrossi A (2009) A simple procedure to improve the pressure evaluation in hydrodynamic context using the SPH. Comput Phys Commun 180(6):861–872. https://doi.org/10.1016/j.cpc.2008.12.004
41. Fourtakas G, Dominguez JM, Vacondio R, Rogers BD (2019) Local uniform stencil (lust) boundary condition for arbitrary 3-d boundaries in parallel smoothed particle hydrodynamics (sph) models. Comput Fluids 190:346–361. https://doi.org/10.1016/j.compfluid.2019.06.009
42. Monaghan JJ, Cas RAF, Kos AM, Hallworth M (1999) Gravity currents descending a ramp in a stratified tank. J Fluid Mech 379:39–69. https://doi.org/10.1017/S0022112098003280
43. Crespo AJC, Gómez–Gesteira M, Dalrymple RA (2007) Boundary conditions generated by dynamic particles in SPH methods. Comput Mater Continua 5(3):173–184. https://doi.org/10.3970/cmc.2007.005.173
44. Zhang F, Crespo A, Altomare C, Dominguez J, Marzeddu A, Shang S, Gomez-Gesteira M (2018) DualSPHysics: a numerical tool to simulate real breakwaters. J Hydrodyn 30(1):95–105. https://doi.org/10.1007/s42241-018-0010-0
45. González-Cao J, Altomare C, Crespo AJC, Domínguez JM, Gómez-Gesteira M, Kisacik D (2019) On the accuracy of dualsphysics to assess violent collisions with coastal structures. Comput Fluids 179:604–612. https://doi.org/10.1016/j.compfluid.2018.11.021
46. English A, Domínguez JM, Vacondio R, Crespo AJC, Stansby PK, Lind SJ, Chiapponi L, Gómez-Gesteira M (2021) Modified dynamic boundary conditions (mDBC) for general purpose smoothed particle hydrodynamics (SPH): application to tank sloshing, dam break and fish pass problems. Comput Part Mech. https://doi.org/10.1007/s40571-021-00403-3
47. Liu MB, Liu GR (2006) Restoring particle consistency in smoothed particle hydrodynamics. Appl Numer Math 56(1):19–36. https://doi.org/10.1016/j.apnum.2005.02.012
48. Capasso S, Tagliafierro B, Güzel H, Yilmaz A, Dal K, Kocaman S, Viccione G, Evangelista S (2021) A numerical validation of 3D experimental dam-break wave interaction with a sharp obstacle using DualSPHysics. Water. https://doi.org/10.3390/w13152133
49. Monaghan JJ, Kos A, Issa N (2003) Fluid motion generated by impact. J Waterway Port Coastal Ocean Eng 129(6):250–259. https://doi.org/10.1061/(ASCE)0733-950X(2003)129:6(250)
50. Project Chrono Development Team. Chrono: An Open Source Framework for the Physics-Based Simulation of Dynamic Systems. https://github.com/projectchrono/chrono. Accessed 07 May 2020
51. Sunday C, Murdoch N, Tardivel S, Schwartz SR, Michel P (2020) Validating N-body code Chrono for granular DEM simulations in reduced-gravity environments. Mon Not R Astron Soc 498(1):1062–1079. https://doi.org/10.1093/mnras/staa2454
52. Bauchau OA, Craig JI (2009) Euler–Bernoulli beam theory. Springer Netherlands, Dordrecht, pp 173–221. ISBN 978-90-481-2516-6. https://doi.org/10.1007/978-90-481-2516-6_5
53. Heng P, Alhasawi A, Battini JM, Hjiaj M (2019) Co-rotating rigid beam with generalized plastic hinges for the nonlinear dynamic analysis of planar framed structures subjected to impact loading. Finite Elem Anal Des 157:38–49. https://doi.org/10.1016/j.finel.2018.11.003
54. Liao K, Hu C, Sueyoshi M (2015) Free surface flow impacting on an elastic structure: experiment versus numerical simulation. Appl Ocean Res 50:192–208. https://doi.org/10.1016/j.apor.2015.02.002

55. Antoci C, Gallati M, Sibilla S (2007) Numerical simulation of fluid–structure interaction by SPH. Comput Struct 85(11–14), 879–890. https://doi.org/10.1016/j.compstruc.2007.01.002
56. Monaghan JJ (2000) SPH without a tensile instability. J Comput Phys 159(2):290–311. https://doi.org/10.1006/jcph.2000.6439